Computational study of transient shear banding in soft jammed solids

Vishwas V. Vasisht [1,2] and Emanuela Del Gado [2]

[1] *Indian Institute of Technology Palakkad, Ahalia Integrated Campus, Kozhippara P.O. — Palakkad, Kerala 678557, India*

[2] *Department of Physics, Institute for Soft Matter Synthesis and Metrology, Georgetown University, 37th and O Streets, N.W., Washington, DC 20057, USA*

(Received 18 August 2019; revised 11 May 2020; accepted 29 May 2020; published 6 July 2020)

We have designed three-dimensional numerical simulations of a soft spheres model, with size polidispersity and in athermal conditions, to study the transient shear banding that occurs during yielding of jammed soft solids. We analyze the effects of different types of drag coefficients used in the simulations and compare the results obtained using Lees-Edwards periodic boundary conditions with the case in which the same model solid is confined between two walls. The specific damping mechanism and the different boundary conditions indeed modify the load curves and the velocity profiles in the transient regime. Nevertheless, we find that the presence of a stress overshoot and of a related transient banding phenomenon, for large enough samples, is a robust feature for overdamped systems, where their presence do not depend on the specific drag used and on the different boundary conditions.

DOI: 10.1103/PhysRevE.102.012603

I. INTRODUCTION

Solids whose microscopic constituents are densely packed into an amorphous assembly and basically insensitive to thermal fluctuations form an integral part of our everyday life, with examples ranging from pharmaceutical, cosmetic, and food products to wet cement. Understanding the flow properties of such materials is therefore of technological importance while raising a number of fundamental questions [1–3]. Under shear deformations, these materials flow only when the applied shear stress is above a threshold value, the yield stress. As the imposed strain increases at a fixed shear rate, they show an initial linear increase in the stress, often followed by a stress overshoot, beyond which the system yields before reaching a steady flow state [4–7]. The steady-state shear stress (σ) as a function of the applied shear rate ($\dot{\gamma}$) provides a constitutive behavior (flow curve) that in most cases is well described by the Herschel-Bulkley (HB) curve $\sigma = \sigma_Y + \kappa\dot{\gamma}^n$, where the yield stress σ_Y, the effective viscosity κ, and the exponent n are in principle material specific [8,9]. The constitutive behavior under flow is interesting in itself and has been the subject of many investigations [10–16], but here we are interested instead in the transient behavior of the material before it reaches the steady-state flow, where it maintains features of both its solid and fluid response. Before reaching the steady flowing state, in fact, jammed soft solids often display flow instabilities which manifest in terms of strong spatial inhomogeneities in the flow profile even when the material is homogeneously driven, a phenomenon often referred to as shear localization or shear banding.

Shear banding in complex fluids like polymer solutions and wormlike micelles has been extensively studied, and in many cases its origin is understood in terms of flow alignment of the microstructure [17] or flow-induced crystallization [18]. The theoretical approaches used typically couple the flow fields with the microstructure [3,17,19–21]. In jammed and soft glassy materials, these phenomena are less understood and the subject of intense investigations [3,5,6,13,22–28]. The questions of interest overlap with the physics of jamming [2,12,29] and the rheology of soft matter [13,22,23,26], granular assemblies [30–36], or glasses [7,11,37]. The possible association of flow inhomogeneities to underlying nonequilibrium phase transitions is increasingly debated [38–43], and a good understanding of their microscopic origin is fundamentally lacking, especially when the shear banding is observed as a transient feature that does not persist in steady state [5–7,24].

Microscopic computer simulations can be effective in bringing new insight, but most of the existing studies have been performed in two dimensions and in the quasistatic limit (i.e., zero shear rate) while experiments are always performed at finite shear rates and nearly always in three dimensions. Together with mesoscale simulations based on elasto-plastic models [13,16], most of the existing microscopic simulation studies have focused on the part of the phenomenon that can be rationalized in terms of the emergence of local plastic rearrangements in an elastic background [11]. That is, they do not capture the coupling of the microscopic dynamics to the imposed deformation rate. Recent works, instead, have pointed precisely to the crucial role of the rate-dependent dynamics, calling for dedicated numerical investigations [5,24,44]. Computational studies with finite deformation rates can be very sensitive to the specific treatment of viscous forces close to jamming [45], but, for shear banding detected in jammed dense suspensions [46–48], there is little clarity on which results may depend on the microscopic dissipation or the boundary conditions used.

To be able to address such questions, we have devised a numerical study using three-dimensional (3D) microscopic simulations and finite deformation rates. In this paper we analyze the outcomes for the shear start-up response under varying shearing protocols and boundary conditions, with the goal to extract the robust features that do not depend on the specifics of the numerical simulations. We study a

jammed suspension (at volume fraction $\phi \simeq 0.7$) of polydisperse spheres with soft repulsive interactions, i.e., a deeply jammed soft amorphous solid. We find that the shear start-up is characterized by a stress overshoot and formation of a transient band, which eventually disappears upon reaching the steady state. We extensively test whether such findings depend on different implementations of the viscous drag due to the background solvent or on different types of boundary conditions. Our study indicates that the stress overshoot and the shear banding during the shear start-up are robust features emerging from the microscopic physics of our model material, they do not qualitatively change with the different shearing protocols used here and are mainly controlled by the sample age that we can change through the preparation protocol.

The paper is organized as follows. In Sec. II we discuss the model system and the sample preparation protocol as well as the rheological and structural characterization of the initial sample configurations. In Sec. III we discuss the shearing protocols followed in our work for performing finite shear rate simulations. Sections IV and V contain the results comparing the transient rheological properties obtained from different protocols. At the end, in Sec. VI we present conclusions and discussion.

II. MODEL AND SAMPLE PREPARATION

The 3D model for soft amorphous material we investigate is composed of a non-Brownian suspension of soft repulsive particles interacting via a truncated and shifted Lennard-Jones potential [49], given by $U(r) = 4\epsilon[(a_{ij}/r_{ij})^{12} - (a_{ij}/r_{ij})^{6}] + \epsilon$, for $r_{ij} \leqslant 2^{1/6}a_{ij}$, else $U(r_{ij}) = 0$. Here ϵ is the unit energy in the simulations, r_{ij} being the center-to-center distance between the particle i and j, and $a_{ij} = 0.5(a_i + a_j)$, with a_i and a_j being the diameter of particles i and j, respectively. The diameters of the particles are drawn from a Gaussian distribution with variance of 10%, whose mean is used as unit length a. All the simulations are performed at a volume fraction $\phi \approx 70\%$, consisting of 10^5 (97 556) particles (unless otherwise mentioned). Albeit simple, this type of model has been successfully used for numerical simulations of soft solids in various contexts and proven to capture the fundamental physics of their behavior under deformation [7,15,27,37,47]. Rheological studies in the literature using Hertzian or harmonic interactions [27,50] or other types of soft potentials [7,50] show that the details of the interaction potentials have little impact on the results obtained at these volume fractions.

We prepare the numerical samples to be sheared using the following procedure. An initial FCC crystal at the chosen volume fraction of 0.70 (with $lx = ly = lz = 42.18a$) is melted at $T = 5.0\epsilon/k_B$ and equilibrated at the same temperature using NVT molecular dynamics (MD) for $\simeq 5 \times 10^4$ MD steps, with a MD time step of $\Delta t = 0.001\tau_0$ (where $\tau_0 = \sqrt{ma^2/\epsilon}$ is the unit of time and m is the unit mass). After making sure that there is no signature of crystallinity in the equilibrated sample by measuring the bond orientational order parameter Q_6 [51], the melt is subjected to a systematic temperature quench. From the initial temperature of $T = 5.0\epsilon/k_B$ we decrease the system temperature by ΔT, after which we let the system relax at the temperature $T - \Delta T$ for 10^4 MD steps. We repeat this procedure several times, until $T = 0.001\epsilon/k_B$ is reached.

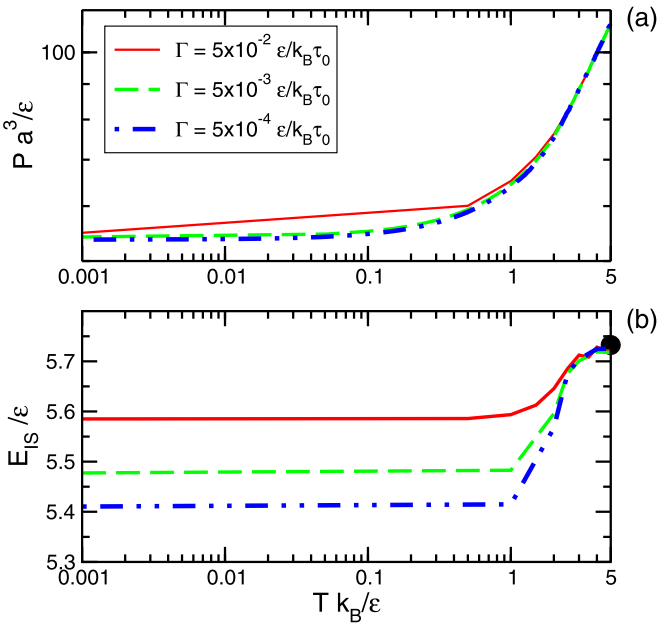

FIG. 1. (a) Pressure computed as a function of temperature for samples quenched at that temperature with different cooling rates. (b) The inherent structure energy as a function of temperature for different cooling rates: Deeper basins of the potential energy landscape are accessed with decreasing cooling rate.

By changing the ΔT we control the cooling rate Γ. The samples discussed here have been prepared for Γ corresponding to $5 \times 10^{-2},\ 5 \times 10^{-3},\ 5 \times 10^{-4}\epsilon/(k_B\tau_0)$. After the system reaches $T = 0.001\epsilon/k_B$, we perform an energy minimization using the conjugate gradient (CG) method to take the system to the zero temperature limit. For the fastest quench rate case, we minimize the energy directly from the equilibrium liquid state at $T = 5.0\epsilon/k_B$ using CG. Following the above described protocol we prepare five independent samples at each cooling rate (except for the lowest one, where we have three samples). The initial configurations so obtained are subjected to shear deformation at a finite shear rate. Before studying the shear start-up behavior we carefully analyze various properties of the initial sample configurations.

In Fig. 1(a) we show the pressure measured as a function of the temperature as the sample is quenched at a chosen cooling rate Γ. The pressure dependence on the temperature does not change with Γ until $T = 3.0\epsilon/k_B$, which in our model corresponds to the onset of glassy dynamics. Below such an onset temperature, the pressure achieved through our cooling protocol decreases with decreasing Γ. In Fig. 1(b) we plot the energy of the closest local minimum accessible to the system, obtained through CG, as a function of T. One can clearly see that, upon decreasing Γ, we access deeper local minima (or inherent structures) of the total potential energy [52–55] below the onset temperature. We next characterize the mechanical and structural properties of these inherent structure configurations obtained from different Γ.

In most amorphous materials, solid properties do not emerge from strictly random packings because the microscopic (interparticle) forces at play during solidification introduce correlations and mechanical heterogeneities [56].

Our preparation protocol uses the cooling rate to include history-dependent processes that develop during solidification. In this respect, our approach is different from what is done in simulation studies of granular assemblies where the samples are specifically prepared to be as close as possible to the onset of jamming [31,34,57,58] or rapidly quenched through CG [59,60]. We are far beyond jamming and systematically change the cooling rate to investigate how structural correlations and mechanical heterogeneities, developed upon cooling, change the linear response of the materials as well as the rate-dependent yielding. Recent studies that have started to explore more aged samples in the context of ultra-stable or ultra-aged glasses may have a similar scope [61].

A. Linear viscoelastic response of the initial configurations

In order to characterize the mechanical properties of the initial configurations, we compute the complex modulus by performing small-amplitude oscillatory shear. By applying a shear strain $\gamma(t) = \gamma_0 \sin(\omega t)$, for a strain amplitude of $\gamma_0 = 1\%$, we monitor the stress response for varying frequencies ω [62]. We monitor the energy and pressure evolution during the oscillatory shear cycles, and once the system reaches a saturation in these quantities as a function of the number of cycles, we extract the linear visco-elastic moduli (respectively storage and loss) using

$$G'(\omega, \gamma_0) = \frac{\omega}{\gamma_0 \pi} \int_{t_0}^{t_0 + 2\pi/\omega} \sigma_{xy}(t) \sin(\omega t)\, dt, \tag{1}$$

$$G''(\omega, \gamma_0) = \frac{\omega}{\gamma_0 \pi} \int_{t_0}^{t_0 + 2\pi/\omega} \sigma_{xy}(t) \cos(\omega t)\, dt. \tag{2}$$

In Fig. 2 we show G' $(\omega, \gamma_0 = 0.01)$ and G'' $(\omega, \gamma_0 = 0.01)$ as a function of the applied frequency ω for the initial configuration prepared at a cooling rate $\Gamma = 5 \times 10^{-4} \epsilon / k_B \tau_0$. The data show that the sample is solid, with $G' \gg G''$ at low frequencies, and the zero frequency storage modulus can be extracted by extrapolating the data to $\omega = 0$. When comparing with typical rheological behavior close to the jamming transition [63], the data indicate that the materials prepared using the protocol described above are well beyond the rigidity threshold and that a large number of excess neighbors (with respect to the minimum number required by the isostaticity condition) must contribute to their modulus. We compute the zero frequency storage modulus for samples prepared with different Γ, as shown in the inset of Fig. 2. The arrow in the inset of Fig. 2 corresponds to the fastest cooling rate, where a liquid configuration is directly subjected to CG minimization. With decreasing the cooling rate Γ, the configurations in deeper local minima of the potential energy landscape, as identified in Fig. 1(b), clearly correspond to solids with higher mechanical strength, similar to the results obtained in Ref. [61].

B. Structural analysis

In order to gain insight into the microscopic structural underpinnings, we analyze the structure of the samples by constructing a 3D radical Voronoi tesselation with the VORO++ open source software library [64] and compute the Voronoi

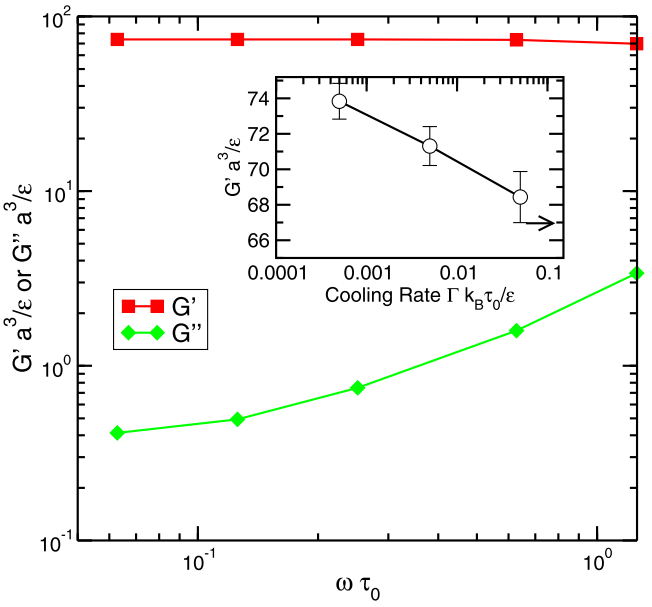

FIG. 2. The complex moduli (elastic, G′, and plasti, G″) computed as a function of frequency for an initial configuration prepared at a cooling rate $\Gamma = 5 \times 10^{-4}$. Inset: The zero frequency storage modulus G′ as a function of cooling rate Γ. The G′ increases with decreasing the cooling rate. The arrow indicates the value computed for the infinitely fast cooling rate, obtained from the CG minimization of a high-T configuration.

polyhedra. This method is well suited for our samples made of polydisperse spheres. For samples prepared at different cooling rate Γ, we obtain the statistics of various Voronoi polyhedra (defined by number of faces, edges, and vertices). If we use the neighbors identified by the Voronoi polyhedra to define the particle contacts, the data confirm that all samples are well in the jammed phase. In Fig. 3 we show the fraction of different polyhedra (which constitute more than 5% of each sample) as a function of the cooling rate. The data show that the fraction of Voronoi dodecahedra is clearly affected by the cooling rate Γ, whereas the contribution of the other polyhedra does not change much. A Voronoi dodecahedron corresponds to a local packing which is an icosahedron, where neighboring particles form an icosahedron around a reference particle. Relatively higher percentages of local icosahedral packing are expected and widely observed in slowly quenched supercooled liquids [65], as well as in glasses, with similar spherically symmetric interactions [66–68].

Having characterized the initial configurations prepared at various Γ, we now analyze the rheological response of these samples subjecting them to a continuous shear deformation at a finite rate.

III. SHEARING PROTOCOLS

The samples characterized as described above are subjected to a shear deformation of strain amplitude $\gamma(t)$ with constant imposed rate $\dot{\gamma}$, either using Lees-Edwards boundary conditions (LEBCs) or using a wall-based (WB) protocol. Note that in all simulations discussed below $[x, y, z]$ refers, respectively, to flow, gradient, and vorticity directions. For

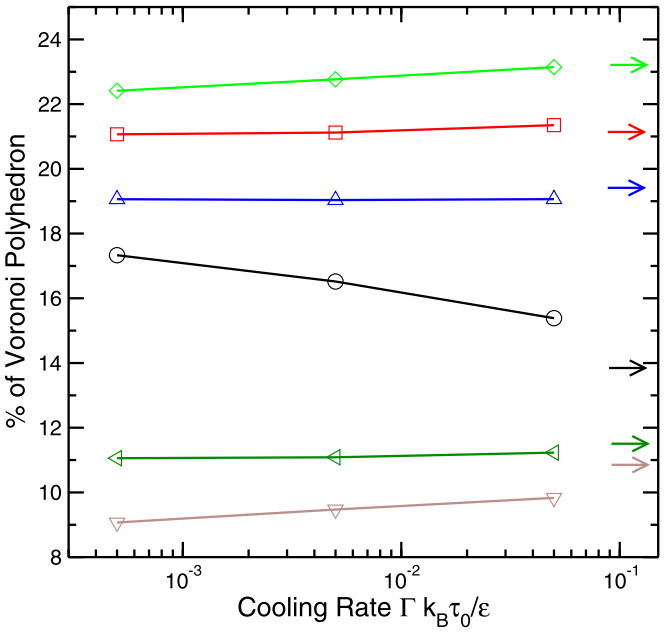

FIG. 3. Fraction of different Voronoi polyhedra in a sample prepared using different cooling rates. In each initial configuration, a Voronoi polyhedron is identified from the number of faces, vertices, and edges, using a Voronoi tesselation analysis. Any polyhedron species that corresponds to at least 5% of the total is considered. Open circles correspond to Face (F) = 12, Edges (E) = 30, and Vertices (V) = 20, a Voronoi dodecahedron, or a particle with icosahedron neighbors. Likewise, squares (F = 13; E = 33; V = 22), diamonds (F = 14; E = 36; V = 24), up-side triangles (F = 15; E = 39; V = 26), left-side triangles (F = 16; E = 42; V = 28), and down-side triangles (F = 17; E = 45; V = 30). The arrow denotes the data for the infinitely fast cooling rate, obtained from conjugate gradient minimization.

LEBCs we start from a cubic simulation box. The number of particles $N = 97\,556$, and the box dimensions are $l_x = l_y = l_z = 42.18a$. For the WB protocol, the top wall is moved at chosen velocity associated with the applied shear rate, while the bottom wall is kept fixed. We confine the sample in the y direction by freezing two layers of particles at the simulation box boundary. l_y is the width of the box in the y direction for the confined samples. In this case $l_x = l_z = 42.1798a$, $l_y = 37.18a$, and $N = 85\,992$. All shear rates are measured in units of τ_0^{-1}.

For the LEBC we solve the equations of motion in two different ways. In the first way, which in the following is called LEBC1, we use the following dissipative particles dynamics (DPD) equations of motion [69]:

$$m\frac{d^2\vec{r}_i}{dt^2} = -\zeta_{DPD}\sum_{j(\neq i)}\omega(r_{ij})(\hat{r}_{ij}\cdot\vec{v}_{ij})\hat{r}_{ij} - \vec{\nabla}_{\vec{r}_i}U, \qquad (3)$$

where m is the mass of the particle and the first term in the right-hand side (RHS) is the damping force, which depends on the damping coefficient ζ_{DPD}. The relative velocity $\vec{v}_{ij} = \vec{v}_j - \vec{v}_i$ is computed over a cutoff distance $r_{ij} \leqslant 2.5a_{ij}$, with the weight factor $\omega(r_{ij}) = 1$. These choices for the cutoff distance and the weight factor are consistent with other studies in the literature for similar systems [29,69–71]. In the viscous damping we have considered only the radial contribution of the relative velocities, since the particles are pointlike and the main sources of change in the velocity are the interparticle forces which are purely radial [72]. Nevertheless, the tangential contribution to the damping forces can also be included as $[(\hat{r}_{ij}\cdot\vec{v}_{ij})\hat{r}_{ij}) + (\vec{v}_{ij} - (\hat{r}_{ij}\cdot\vec{v}_{ij})\hat{r}_{ij}]$ [45]. In most of this work we have used the formulation with only the radial contribution, but in one of the following sections we briefly discuss the effect of including the transverse term, which has also been investigated recently in Ref. [73]. The second term in the RHS is the conservative force due to the interactions between particles.

In the second way, which we indicate as LEBC2, we solve equations of motion where the solvent drag is Stokes-like and depends only on the particle velocity relative to a background, affine flow [46,74–76], as in a free-draining approximation, given by

$$m\frac{d^2\vec{r}_i}{dt^2} = -\zeta_{SD}\left(\frac{d\vec{r}_i}{dt} - \dot{\gamma}y_i\vec{e}_x\right) - \vec{\nabla}_{\vec{r}_i}U, \qquad (4)$$

where again m is the particle mass and the first term in the RHS is the damping force, which depends on the damping coefficient ζ_{SD}. Hence the drag force is proportional to the difference between the particle's velocity $d\vec{r}_i/dt$ and an affine background velocity, dictated by imposed shear rate, given by $\dot{\gamma}y_i\vec{e}_x$. The second term in the RHS is the force due to the interactions between particles. While one concern with this second approach is that it does not strictly conserve momentum (i.e., it is not Galileian-invariant) [70,77], its use can still be justified in systems where most of the stress induced through the imposed deformation is due to interparticle interactions and the contribution of the solvent is a minor correction. This type of drag term allows for simpler and faster simulations, with no need to adjust additional parameters such as the cutoff or the form of the weight factor in the DPD one. We will show in the following that this free-draining approximation may work well in the case of deeply jammed systems such as those of interest here.

For the WB shear deformation tests, we follow the procedure of Varnik and co-workers in Ref. [4]. Two walls confine the samples along the direction $\hat{y}$, at a relative distance l_y: one wall moves at a velocity $\vec{v} = v_x^{\text{wall}}\hat{x} = \dot{\gamma}l_y\hat{x}$, while the other is kept fixed. The particles that form the wall are completely frozen during the evolution of the system, but the interactions between the wall and the sample particles are the same as in the sample. For the WB shear deformation we use only the DPD approach as in Eq. (3). In fact, if the drag coefficient is directly proportional to the particle velocity as in Eq. (4), in the WB simulations the particles near the moving wall feel more drag than the ones away from it. As a consequence, for large samples the time needed for particles near to the nonmoving wall to sense the deformation is quite long (i.e., quite larger than the sound speed in the system). This behavior could be mistaken for a shear banding, but it is only a numerical artifact due to the use of Eq. (4) in this geometry and disappears using the DPD equation (3) instead.

Finally, both Eqs. (3) and (4) include the particle inertia since this allows us to use the same efficient and precise

algorithms devised for MD [78]. Nevertheless we can effectively study the dynamics in the overdamped limit regime by suitably adjusting the damping coefficients ζ_{SD} and ζ_{DPD}. As a measure of the extent of damping, we can define an inertial quality factor $Q = \tau_{damp}/\tau_{vib}$, that measures the ratio between the timescale over which the inertial motion is damped $\tau_{damp} = m/\zeta$, due to the solvent drag, and the timescale $\tau_{vib} = \sqrt{ma^2/\epsilon}$ over which a particle of mass m and diameter a is accelerated by the force ϵ/a. For a fully overdamped system $Q \to 0$. It has been shown that for the athermal conditions considered here, and for similar types of interactions, $Q \approx 1$ well approximates the overdamped regime [69,79]. Hence here we focus on $Q \approx 1$ and show also that the results we obtained do not vary significantly by decreasing Q or varying it around 1. As stated above, the shear rates in the following are always expressed in units $\tau_0^{-1} \equiv \tau_{\rm vib}^{-1}$.

All simulations have been performed using LAMMPS molecular dynamics package [80], with modifications to the source code to incorporate continuous polydisperse interactions, since we use a distribution of particle sizes and the interaction shape depends on the particle diameters. In Fig. 4 we show a rendering of samples prepared at $\Gamma = 5 \times 10^{-4}\epsilon/(k_B\tau_0)$ and sheared at $\dot\gamma = 10^{-4}\tau_0^{-1}$ (the snapshots are both taken at $\gamma = 0.12$, during the stress decay) using LEBC1 and WB protocols with $Q = 1$. We use the color scheme to show the velocities of the particles, which vary between $0\ a/\tau_0$ (white) and $0.005\ a/\tau_0$ (black).

In the following section we present a comparative study of the rheological response starting from the load curves, using the two different boundary conditions and the two different equations of motion introduced above.

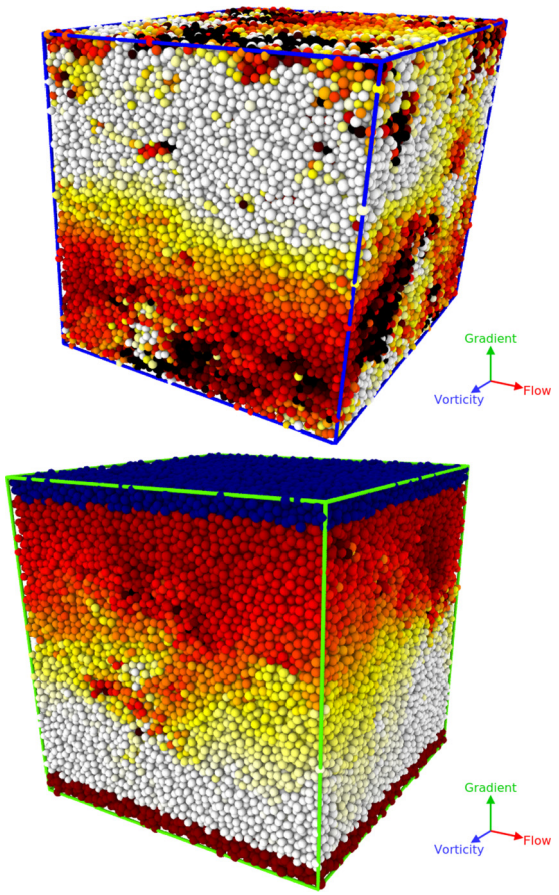

FIG. 4. Simulation rendering of samples prepared at $\Gamma = 5 \times 10^{-4}\epsilon/(k_B\tau_0$ and sheared at $\dot\gamma 10^{-4}\tau_0^{-1}$ using LEBC1 (top) and WB (bottom) protocol. We use the hot color gradient scheme based on the velocities of the particles, which vary between $0\ a/\tau_0$ (white) and $0.005\ a/\tau_0$ (black). In the WB protocol the top wall (dark blue particles) is moved at a velocity given by the applied shear rate, while the bottom wall (maroon particles) is kept fixed.

IV. LOAD CURVES AND FLOW PROFILES: COMPARISON OF THE DIFFERENT SHEARING PROTOCOLS

We begin with the rheological data obtained for a sample prepared at cooling rate $\Gamma = 5 \cdot 10^{-4}\epsilon/(k_B\tau_0)$, i.e., a well-annealed sample, and for a sample obtained by directly minimizing the energy of the high-temperature fluid with CG, i.e., a poorly annealed sample. Both samples are sheared at $\dot\gamma = 10^{-4}\tau_0^{-1}$ and $\dot\gamma = 10^{-2}\tau_0^{-1}$, using the different protocols discussed above. All data in this section correspond to the overdamped limit, with the inertial quality factor $Q = 1$. Since all the simulations are performed in athermal conditions, the shear stress is computed from the virial stress tensor $\sigma_{\alpha\beta} = \frac{1}{V}\sum_i \sum_{j>i} r_{ij}^{\alpha} f_{ij}^{\beta}$, where $V(=l_x \times l_y \times l_z)$ is the volume of the system, r_{ij} represents the distance between particle i and j, and f_{ij} is the force on the particle i due to particle j and $\alpha, \beta \in x, y, z$. We indicate the shear component of the stress σ_{xx} with σ, and the virial pressure is obtained as $P = \frac{1}{3}(\sigma_{xx} + \sigma_{yy} + \sigma_{zz})$. The first normal stress difference is computed as $\sigma_{11} = \sigma_{xx} - \sigma_{yy}$.

In Fig. 5 we show load curves, i.e., the shear stress σ versus applied strain γ, for the three different protocols (LEBC1, LEBC2, and WB) and for the two different samples (the well-annealed one and the poorly annealed one mentioned above), sheared at $\dot\gamma = 10^{-4}\tau_0^{-1}$, a relatively low shear rate, and $\dot\gamma = 10^{-2}\tau_0^{-1}$, a higher shear rate. At low shear rate, all the protocols show comparable load curves. For the well-annealed sample, independent of the protocol used, we find that the initial linear regime is followed by a stress overshoot before reaching a steady-state value [see Fig. 5(a)]. The height of the overshoot depends on the age of the sample (as discussed in Sec. VI), and the samples obtained with the highest possible cooling rate, i.e., by rapidly quenching the liquid configuration via CG, do not show any overshoot [see Fig. 5(c)]. Consistent with the discussion in Sec. II A, the response of these poorly annealed samples is more similar to what is typically observed in granular systems [58].

At higher shear rates [see Figs. 5(b) and 5(d)], the load curves confirm the overall tendency that better aged samples have a more pronounced overshoot, and that the decay of the stress from the overshoot becomes steeper with the age [38]. The load curves also show, however, that at a higher shear rate the dependence on the shear protocol is much more prominent. In particular, when comparing LEBC1 and WB at a high rate, we note that the difference in the boundary conditions does not seem to affect the value of the stress overshoot or that of the steady-state value, which instead clearly change with changing the damping mechanism (LEBC1 vs LEBC2).

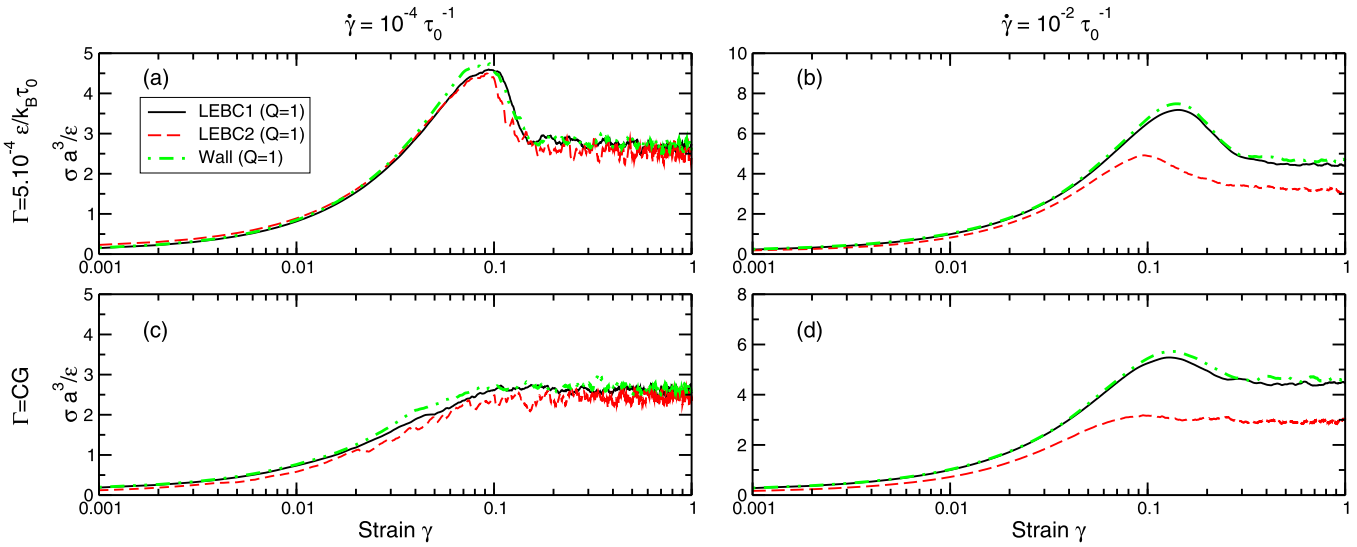

FIG. 5. Load curves obtained at shear rate $\dot{\gamma} = 10^{-4}\tau_0^{-1}$ [left panels, (a) and (c)] and at $\dot{\gamma} = 10^{-2}\tau_0^{-1}$ [right panels, (b) and (d)] for initial configurations prepared at slow cooling rate (top panels) and at an infinitely fast cooling rate (bottom panels). The data are from the LEBC1, LEBC2, and WB protocols.

Comparing the values of shear stresses between the left and right panels in the figure, the dependence of the data obtained for LEBC2 on the shear rate seems to be weaker, in this range of shear rates. These results overall suggest that the protocol LEBC2 (that uses the Stokes drag) allows for relatively less stress accumulation upon increasing the shear rate. They also suggest that the choice of the dissipation mechanism may be more crucial when investigating the banding phenomenon at higher rates. We also note that, approaching the steady state, the stress fluctuations are larger in the case of LEBC2 compared to LEBC1 and WB.

From the load curves we now turn to the local properties by analyzing the velocity profiles of our samples, at different locations along the load curve. The well-aged samples, when sheared at a low shear rate, display a pronounced shear banding that is not detected in the samples prepared with CG and sheared at higher rates. In the wall-driven simulations, the bands nucleate near the walls. With LEBC, there is no such bias, and the flowing band can form anywhere in the system, as long as the system is big enough to accommodate it, as we indeed observe in the simulations [47]. Figures 6, 7, and 8 show the velocity profiles, respectively, obtained with the LEBC1, LEBC2, and WB protocols from the same initial configurations for $\dot{\gamma} = 10^{-4}\tau_0^{-1}$. For different regimes in the load curves [Figs. 6(a), 7(a), and 8(a)], we show the associated velocity profiles in Figs. 6(b), 7(b), and 8(b) (i–ix). The velocity profiles are computed over a strain window of $\Delta\gamma = 0.02$. In spite of some differences in the details of the velocity profiles, we can recognize the following features for all the shearing protocols considered. (1) In the linear response regime of the load curve (i–ii), the velocity profiles show a homogeneous flow with local shear rates (obtained as the slope of the velocity profile) similar to the applied shear rate. (2) In the vicinity of the stress overshoot (iii) a flow instability develops, as indicated by the deviation from the linear velocity profile. Following the stress overshoot, the stress decays back, with $d\sigma/d\gamma < 0$, and in this region we find a back-flow in the system as the velocity profiles show a negative slope [5,81]. We note that the width of the flowing band seems to be set by the amount of back-flow in the system (iv). (3) Upon further shearing, the width of the band grows, and eventually the whole system flows homogeneously. The shear component of the stress has a much weaker (although non-negligible) dependence on the strain. The pressure evolution with γ clearly shows that also the saturation of the normal components of the stress tensor happens only once the profile returns to be homogeneous [Figs. 6(c), 7(c), and 8(c)] [19,24].

When analyzing the local packing through the Voronoi tessellation, we find that the fraction of icosahedrally packed particles has a similar trend. Figure 6(d) shows, for the LEBC1 protocol, how the fraction of icosahedrally packed particles evolves with the increasing strain, and the time required for it to saturate is consistent with the vanishing of the transient shear banding. The connections between the evolution of the local packing and that of the shear inhomogeneities, as well as their dependence on the shear rate, have been thoroughly investigated in Ref. [47]. We also find that the evolution of the system during the shear banding, is accompanied by a positive first normal stress difference ($\sigma_{xx} - \sigma_{yy}$), indicating the presence of dilation. The first normal stress difference, although quite noisy, also seems to grow as the bands develop, and saturate when the flow becomes homogeneous [see Fig. 6(e)]. When comparing further the different protocols across Figs. 6–8, we note that in WB the shear bands always nucleate near the walls and that the time taken to reach an homogeneous flow state is slightly longer than in LEBC1 and LEBC2.

We conclude that the features identified above, i.e., the stress overshoot, the formation and disappearing of the shear banding, and its correlation with the evolution of the normal stresses and with the changes in the local packing, are robust across the different protocols utilized. Hence they are not the

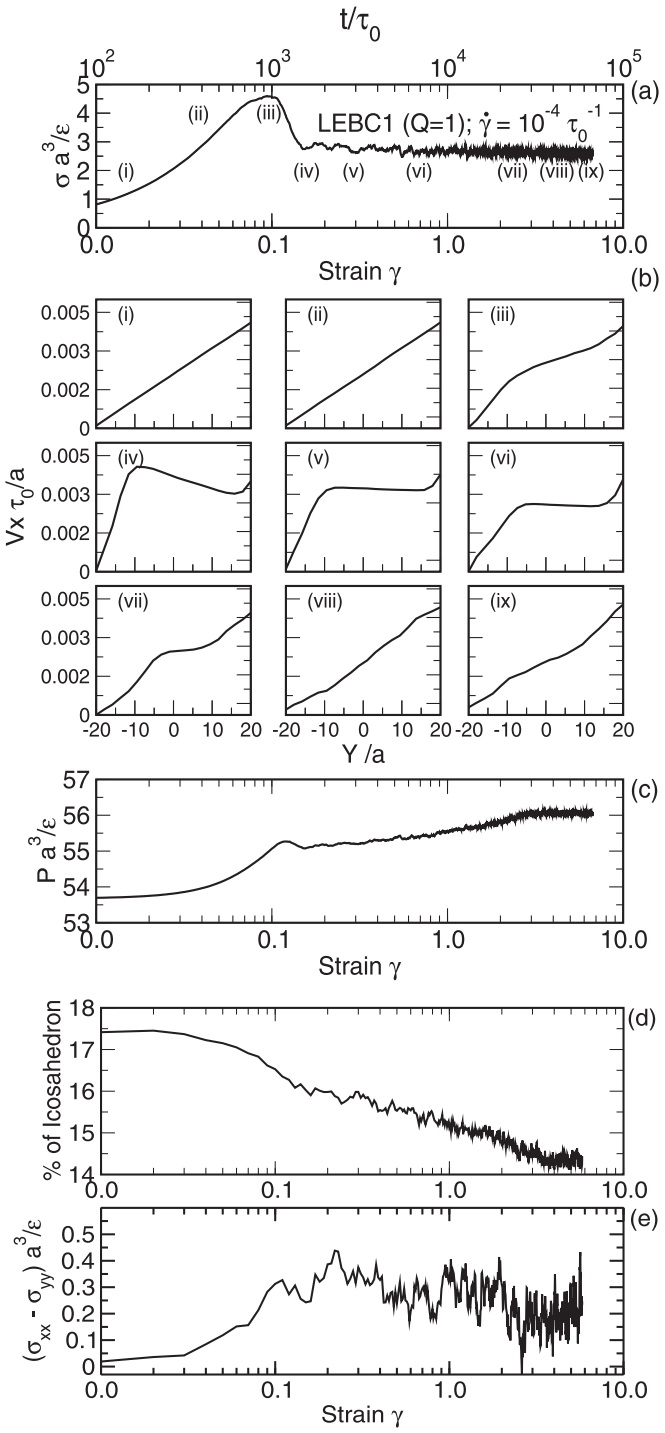

FIG. 6. (a) The load curve obtained using the LEBC1 (pairwise dissipation) protocol, for $Q = 1$, at shear rate $\dot{\gamma} = 10^{-4}\tau_0^{-1}$ for a sample initially prepared at cooling rate $\Gamma = 5 \times 10^{-4}\epsilon/(k_B\tau_0)$. (b) The velocity profile as a function of the coordinate in the gradient direction at points (i–ix) of the load curve. (c) The variation of pressure as a function of the strain over the same range of strain as in the load curve. (d) The first normal stress difference $(\sigma_{xx} - \sigma_{yy})$ as a function of the strain for the same sample. (e) The fraction of icosahedral packing as a function of the strain.

result of numerical artifacts or specific protocol choices. They are instead inherent of well-aged jammed solids when sheared at sufficiently low rates.

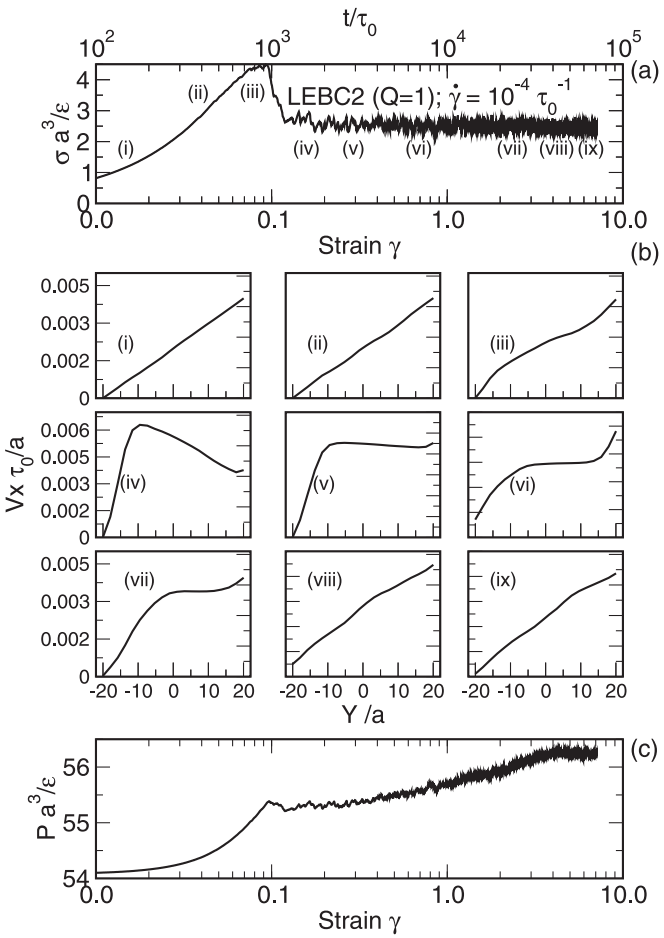

FIG. 7. (a) The load curve obtained using the LEBC2 protocol (Stoke-like dissipation), for $Q = 1$, at shear rate $\dot{\gamma} = 10^{-4}\tau_0^{-1}$ for an initial configuration prepared at cooling rate $\Gamma = 5 \times 10^{-4}\epsilon/(k_B\tau_0)$. (b) The velocity profile as a function of the coordinate in the gradient direction at points (i–ix) of the load curve. (c) The variation of pressure as a function of the strain over the same range of strain as in the load curve. Similar to the results of DPD protocol, the system shows the feature of transient shear banding as well as the decoupling between the stress and pressure.

In the next section we discuss the possible dependence of our findings on the value of the drag coefficient chosen.

V. DEPENDENCE ON DISSIPATION COEFFICIENT

The contribution of inertial terms to the rheology of jammed suspensions has been extensively explored in steady state in Refs. [69,79,82]. Here we address instead how the stress overshoot and the shear banding during the transient preceding the steady state is affected by the dissipation coefficient. To do this, we consider the LEBC1 protocol and vary the value of the coefficient ζ_{DPD} between 2 ($m\tau_0^{-1}$) and 0.01 ($m\tau_0^{-1}$). This means that the inertial quality factor Q defined above varies from 0.5 to 100, i.e., from the case where the damping time is much shorter than the characteristic time of the inertial motion (i.e., the overdamped limit) to a case where it is 100 times longer (underdamped case).

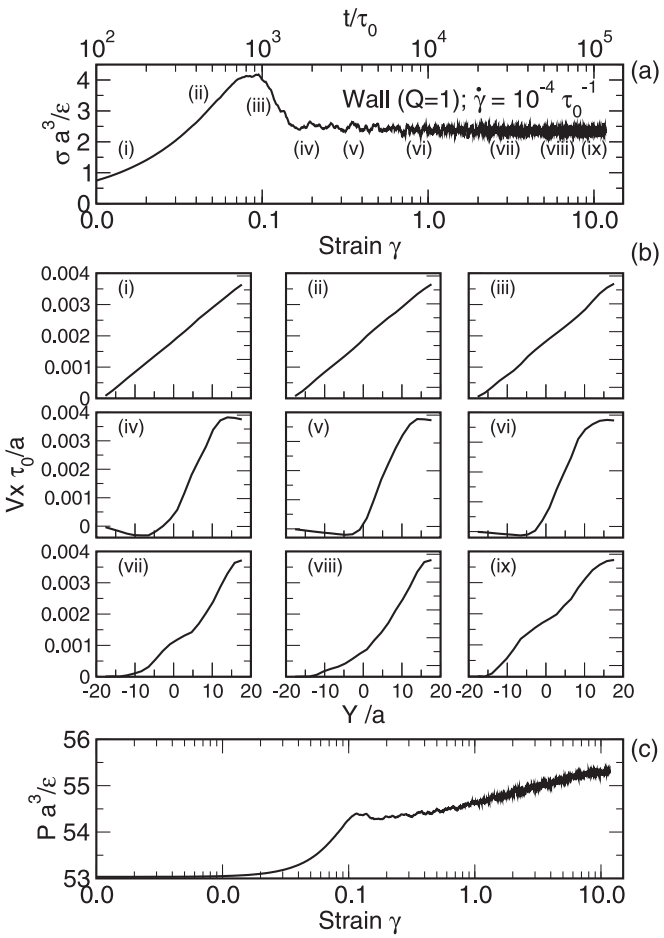

FIG. 8. (a) The load curve obtained from uniform shearing, using the WB protocol, at shear rate $\dot{\gamma} = 10^{-4}\tau_0^{-1}$ for a initial configuration prepared at cooling rate $\Gamma = 5 \times 10^{-4}\epsilon/(k_B\tau_0)$. (b) The velocity profile as a function of the coordinate in the gradient direction at points (i–ix) of the load curve. (c) The variation of pressure as a function of the strain over the same range of strain as in the load curve.

In Refs. [69,79] it has been shown that, with a strongly underdamped dynamics, inertia may qualitatively change the flow properties of a jammed suspension, with the possibility to develop even nonmonotonic flow curves. This is not the case here, where the flow curves remain monotonic, suggesting that for the whole range of Q considered here the high-density and the jammed conditions control the material flow rather than the particle inertia. In Fig. 9(a) we show the load curves of the same well-annealed sample studied with LEBC1, but now with different values of the inertial quality factor Q. The applied shear rate corresponds to $10^{-4}\tau_0^{-1}$. The data show that the initial linear response remains unaffected, and the stress overshoot seems to slightly decrease with the increasing Q. The decay after the overshoot becomes increasingly steeper with increasing Q. If we express the applied shear rate in terms of Weissenberg number ($\mathrm{Wi} = \zeta_{DPD}a^2/\epsilon\dot{\gamma}$), the higher the quality factor, the lower is Wi. As a consequence, one could think of the increasing quality factor Q as a way to reach effectively lower shear rates. One might expect a trivial scaling of the load curves if the load curve is presented in terms of σ vs $\gamma/\dot{\gamma}$, with $\dot{\gamma}$ in terms of Weissenberg number. But since the initial linear response regime is unaffected by the extent of damping, this scaling does not work. The effect of the inertial contribution can be more intricate, with inertia playing a role in increasing the kinetic temperature in the athermal system and hence leading to a softening of the system during shearing [69,79].

In Figs. 9(b)–9(e), we show the velocity profiles related to different Q and computed at a strain $\gamma \approx 0.2$ by averaging over a strain window $\Delta\gamma = 0.02$. In all the cases, as the stress decays from the overshoot, we observe the formation of shear bands.

Finally, in the data of Fig. 9(a) we also show the results obtained in the LEBC1 protocol when including the transverse contribution to the DPD drag, as discussed in Sec. III, to demonstrate that such modification changes slightly the value of the overshoot and the shape of the decay towards the steady state, but it does not modify the general phenomenology of formation of shear band observed [see also the profile shown in Fig. 9(c)].

With the idea to explore further how the specific form of drag used may change the results obtained, we note that in LEBC1 another important variable corresponds to the pairwise dissipation cutoff used in the DPD drag [Eq. (3)]. For the results shown so far, we have chosen such a cutoff to be $2.5a_{ij}$, as done in Ref. [69]. In Fig. 10(a) we plot together the load curves obtained for LEBC1 with the DPD cutoff $2.5a_{ij}$ and $1.5a_{ij}$, along with the results for the LEBC2 protocol. We observe that the linear response regime is unaffected, and so is the values of the stress overshoot. The stress decay from the the overshoot shows instead a dependence on the cutoff chosen. We observe that the results obtained with the LEBC2 protocol approach those for LEBC1 if the DPD cutoff distance goes down towards a particle diameter, consistent with the fact that LEBC2 corresponds to the free-draining approximation. The related velocity profiles are shown in Figs. 10(b)–10(d) (these are computed at $\gamma = 0.2$ and averaged over $\Delta\gamma = 0.02$), indicating that the decay of the overshoot is always associated to the formation of transient shear bands for both values of the DPD cutoff.

Finally, we have also analyzed how the difference or similarities just described depend on the shear rate. We summarize the outcome of this study in Fig. 11, which shows, for the well-annealed sample, the difference between the stress overshoot and the steady-state value of the shear stress as a function of the shear rate, for different protocols as well as for two different damping coefficients for LEBC1. The data indicate that changing Q in the range of values explored here does not significantly affect the results at sufficiently low rates, whereas one should expect to see significant differences upon increasing the shear rate. Note that we have expressed the shear rate in terms of τ_0^{-1}, instead of using a viscous timescale, in order to compare different protocols where viscous terms are handled in different ways. Different protocols show that the occurrence of the stress overshoot (which is essential for the formation of shear bands) is robust, and its dependence on the steady-state stress across different protocols is similar in the whole range of shear rates (the lines through the data in the figure are power-law fits).

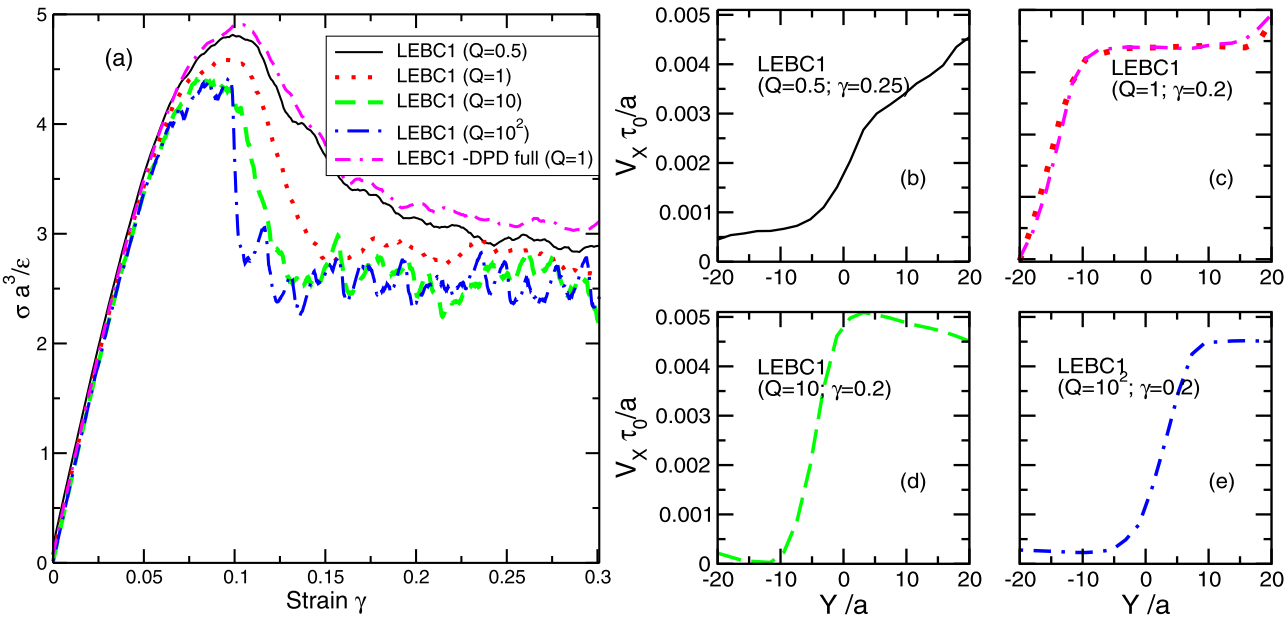

FIG. 9. (a) The load curve obtained from uniform shearing using different dissipation constants, at a shear rate $\dot{\gamma} = 10^{-4}\tau_0^{-1}$, for a initial configuration prepared at $\Gamma = 5 \times 10^{-4}\epsilon/(k_B\tau_0)$. Right panels (b)–(e) show the velocity profile computed in a strain window $\gamma \approx 0.2$, averaged over 2% strain for systems sheared using different dissipation constants. Even in the systems which are relatively underdamped, one finds the formation of shear bands at the vicinity of decay of stress overshoot. These bands are indeed transient in nature, and the damping coefficient would have a bearing on the time required to obtain a homogeneous flow.

VI. DEPENDENCE ON THE SAMPLE AGE

Having explored different treatments of microscopic viscous forces and the effect of different drag coefficients, we want now to emphasize that, at low shear rates, the tendency to have flow inhomogeneity upon yielding is determined mainly by the age of the samples (which determines the stress overshoot and the decay of the shear stress to steady state), due to the different degree of frozen-in stresses [56]. The fact that the stress overshoot depends on the age of the initial solid has been discussed in other studies [5,7,38,47,83]. In

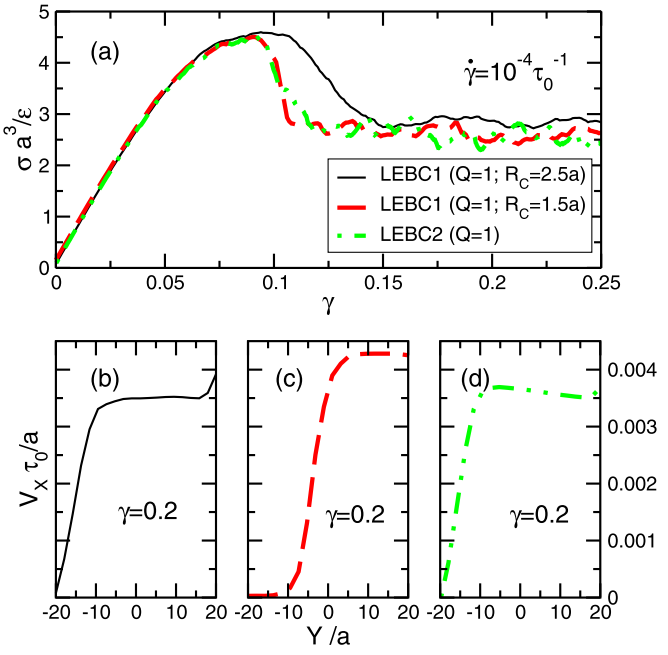

FIG. 10. (a) The load curve obtained from uniform shearing with LEBC1, using DPD cutoff $R_c = 2.5a$ and $R_c = 1.5a$, and with LEBC2, at a shear rate $\dot{\gamma} = 10^{-}4\tau_0^{-1}$, for an initial configuration prepared at $\Gamma = 5 \times 10^{-4}\epsilon/(k_B\tau_0)$. Bottom panels (c)–(d) show the velocity profile, corresponding to the same protocols as in the load curve, computed in a strain window $\gamma \approx 0.2$, and averaged over 2% strain.

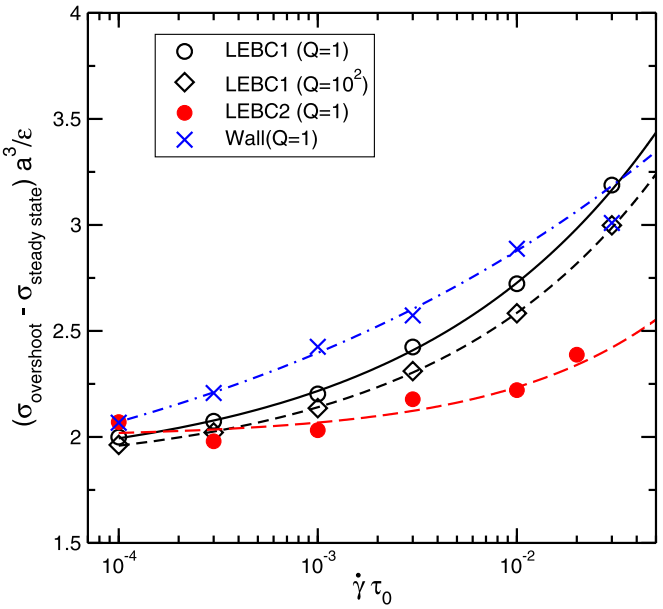

FIG. 11. The difference between the overshoot stress and steady-state stress computed from different shearing protocols and plotted as a function of the shear rate. The lines are power-law fits to the data points.

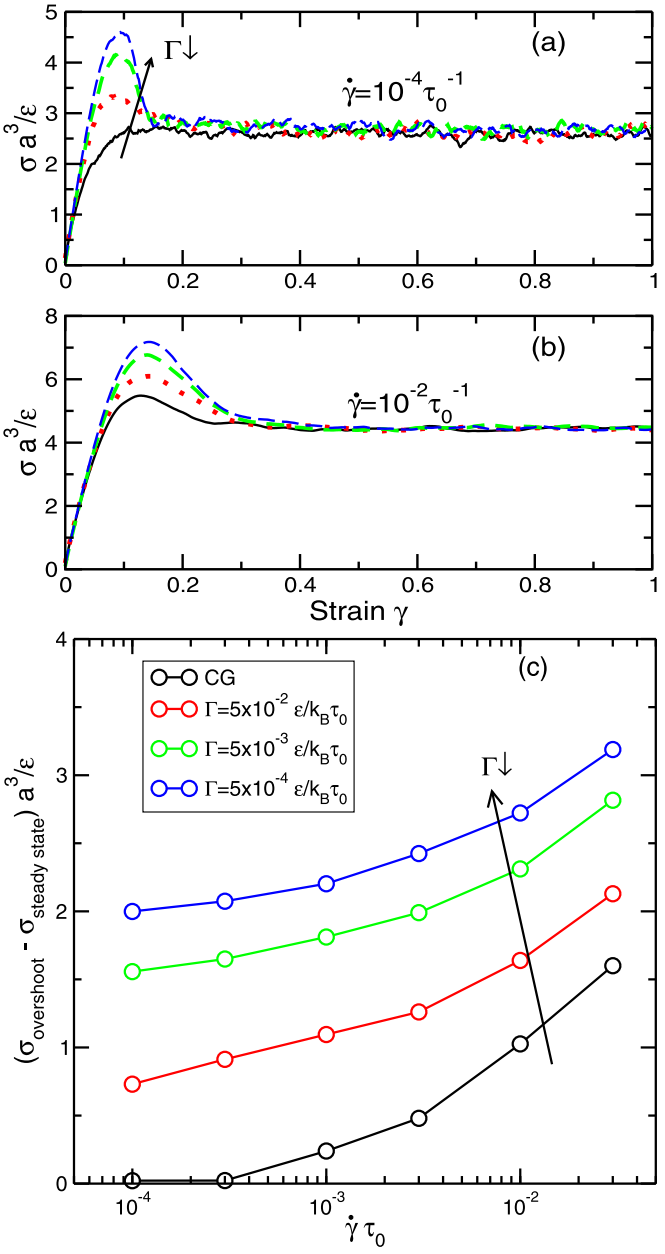

FIG. 12. The load curve for (a) $\dot{\gamma} = 10^{-4}\tau_0^{-1}$ and (b) $\dot{\gamma} = 10^{-2}\tau_0^{-1}$ computed from samples prepared with different cooling rate Γ and using LEBC1. (c) The difference in the overshoot stress and the steady-state stress computed for different sample ages as a function of the applied shear rate, for LEBC1.

the context of the study reported here, we have summarized the dependence of the stress overshoot on the shear rate and on the sample age, in Fig. 12. The data are from the LEBC1 simulations, but the same trends are obtained with the different protocols. The figure also shows the difference between the stress overshoot and the steady-state value of the shear stress as a function of the shear rate, for different cooling rates Γ, corresponding to different sample ages. The results clearly indicate how changing the sample age can qualitatively change the overshoot and its rate dependence. We have investigated how the age of the samples also determines the persistence of the flow inhomogeneities, not only their presence, in Ref. [47]. We refer the reader to that paper for further insights.

VII. CONCLUSIONS

We have devised a 3D numerical study of a jammed suspension of soft spheres, polydisperse in size, under shear. In particular here we have explored different choices for imposing the shear deformation and boundary conditions. We have compared the use of Lees-Edwards boundary conditions with simulations where the samples are confined within walls. We have also compared the use of a DPD drag term to the free-draining approximation (Stokes-like drag). Finally, we have compared simulations with different degrees of inertia, quantified through the inertia quality factor Q. The comparison has been done in terms of load curves and velocity profiles during the transient that leads to the steady-state flow. In all cases, we find that at low rates the shear stress develops an overshoot followed by a relatively long decay (not necessarily gradual) towards the steady-state value. Such a phenomenon is associated to a transient banding with a part of the material that is basically stuck, and the rest flowing. The extended comparison carried on here indicates that these features (the stress overshoot and the transient shear banding) are the genuine results of the emerging response of the material upon yielding and not the consequences of numerical artifacts or unphysical choices in the simulations parameters. When comparing with different approaches currently used, moreover, we find that at low shear rates and in overdamped conditions a Stokes-like drag provides results qualitatively consistent with those of simulations that use a DPD (pairwise) drag term for the load curves, the velocity profiles, and the evolution of the pressure towards the steady state [47]. Our study has been performed in athermal conditions and at volume fractions beyond the jamming transition. Investigating how numerical results of flow inhomogeneities may depend on different dissipation mechanisms for finite temperatures or approaching the jamming transition requires further studies. At finite temperatures, a similar comparison between different types of viscous terms in the equation of motions would be useful, since Stokes-like drag terms or DPD are both applicable, while simulation methods that are specifically suited for homogeneous flow, such as SLLOD [84], may not be appropriate. Closer to jamming, the statistics of avalanches and its dependence on different viscous dissipation mechanisms could provide insights [70,82]. When comparing the different types of drag terms, we have found that the dependence of the stress overshoot, and of the velocity profiles, on the shear rate may be quantitatively different. These findings suggest that numerical studies of the dynamics of the yielding transition could provide results that quantitatively depend on the specific shearing protocol utilized upon increasing the shear rate.

ACKNOWLEDGMENTS

The authors thank Georgetown University and the Swiss National Science Foundation (Grant No. PP00P2 150738) for support.

[1] M. Van Hecke, J. Phys.: Condens. Matter **22**, 033101 (2009).
[2] A. J. Liu and S. R. Nagel, Annu. Rev. Condens. Matter Phys. **1**, 347 (2010).
[3] D. Bonn, M. M. Denn, L. Berthier, T. Divoux, and S. Manneville, Rev. Mod. Phys. **89**, 035005 (2017).
[4] F. Varnik, L. Bocquet, and J.-L. Barrat, J. Chem. Phys. **120**, 2788 (2004).
[5] S. M. Fielding, Rep. Prog. Phys. **77**, 102601 (2014).
[6] T. Divoux, M. A. Fardin, S. Manneville, and S. Lerouge, Annu. Rev. Fluid Mech. **48**, 81 (2016).
[7] G. P. Shrivastav, P. Chaudhuri, and J. Horbach, J. Rheol. **60**, 835 (2016).
[8] P. Hébraud and F. Lequeux, Phys. Rev. Lett. **81**, 2934 (1998).
[9] A. Nicolas, K. Martens, L. Bocquet, and J.-L. Barrat, Soft Matter **10**, 4648 (2014).
[10] J. Goyon, A. Colin, G. Ovarlez, A. Ajdari, and L. Bocquet, Nature (London) **454**, 84 (2008).
[11] A. Lemaître and C. Caroli, Phys. Rev. Lett. **103**, 065501 (2009).
[12] B. P. Tighe, E. Woldhuis, J. J. C. Remmers, W. van Saarloos, and M. van Hecke, Phys. Rev. Lett. **105**, 088303 (2010).
[13] K. Martens, L. Bocquet, and J.-L. Barrat, Soft Matter **8**, 4197 (2012).
[14] J. R. Seth, L. Mohan, C. Locatelli-Champagne, M. Cloitre, and R. T. Bonnecaze, Nat. Mater. **10**, 838 (2011).
[15] V. V. Vasisht, S. K. Dutta, E. Del Gado, and D. L. Blair, Phys. Rev. Lett. **120**, 018001 (2018).
[16] A. Nicolas, E. E. Ferrero, K. Martens, and J.-L. Barrat, Rev. Mod. Phys. **90**, 045006 (2018).
[17] J. K. G. Dhont, Phys. Rev. E **60**, 4534 (1999).
[18] L. T. Shereda, R. G. Larson, and M. J. Solomon, Phys. Rev. Lett. **105**, 228302 (2010).
[19] P. D. Olmsted, Rheol. Acta **47**, 283 (2008).
[20] J. K. Dhont and W. J. Briels, Rheol. Acta **47**, 257 (2008).
[21] S. Lerouge and J.-F. Berret, in *Polymer Characterization-Rheology, Laser Interferometry, Electrooptics*, edited by K. Dusek and J.-F. Joanny, Advances in Polymer Science Vol. 230 (Springer-Verlag, Berlin, Heidelberg, 2010).
[22] L. Bécu, S. Manneville, and A. Colin, Phys. Rev. Lett. **96**, 138302 (2006).
[23] S. Fielding, M. Cates, and P. Sollich, Soft Matter **5**, 2378 (2009).
[24] T. Divoux, D. Tamarii, C. Barentin, and S. Manneville, Phys. Rev. Lett. **104**, 208301 (2010).
[25] R. Besseling, L. Isa, P. Ballesta, G. Petekidis, M. E. Cates, and W. C. K. Poon, Phys. Rev. Lett. **105**, 268301 (2010).
[26] V. Mansard, A. Colin, P. Chauduri, and L. Bocquet, Soft Matter **7**, 5524 (2011).
[27] E. Irani, P. Chaudhuri, and C. Heussinger, Phys. Rev. Lett. **112**, 188303 (2014).
[28] M. Gross and F. Varnik, Soft Matter **14**, 4577 (2018).
[29] N. Xu, C. S. O'Hern, and L. Kondic, Phys. Rev. Lett. **94**, 016001 (2005).
[30] O. Pouliquen, C. Cassar, P. Jop, Y. Forterre, and M. Nicolas, J. Stat. Mech. (2006) P07020.
[31] F. da Cruz, S. Emam, M. Prochnow, J.-N. Roux, and F. Chevoir, Phys. Rev. E **72**, 021309 (2005).
[32] M. Bouzid, M. Trulsson, P. Claudin, E. Clément, and B. Andreotti, Phys. Rev. Lett. **111**, 238301 (2013).
[33] P. Jop, V. Mansard, P. Chaudhuri, L. Bocquet, and A. Colin, Phys. Rev. Lett. **108**, 148301 (2012).
[34] P.-E. Peyneau and J.-N. Roux, Phys. Rev. E **78**, 011307 (2008).
[35] D. L. Henann and K. Kamrin, Phys. Rev. Lett. **113**, 178001 (2014).
[36] A. Favier de Coulomb, M. Bouzid, P. Claudin, E. Clément, and B. Andreotti, Phys. Rev. Fluids **2**, 102301 (2017).
[37] F. Varnik, L. Bocquet, J.-L. Barrat, and L. Berthier, Phys. Rev. Lett. **90**, 095702 (2003).
[38] R. L. Moorcroft, M. E. Cates, and S. M. Fielding, Phys. Rev. Lett. **106**, 055502 (2011).
[39] J. M. Adams, S. M. Fielding, and P. D. Olmsted, J. Rheol. **55**, 1007 (2011).
[40] A. Wisitsorasak and P. G. Wolynes, Proc. Natl. Acad. Sci. USA **114**, 1287 (2017).
[41] G. Parisi, I. Procaccia, C. Rainone, and M. Singh, Proc. Natl. Acad. Sci. USA **114**, 5577 (2017).
[42] M. Ozawa, L. Berthier, G. Biroli, A. Rosso, and G. Tarjus, Proc. Natl. Acad. Sci. USA **115**, 6656 (2018).
[43] M. Popović, T. W. de Geus, and M. Wyart, Phys. Rev. E **98**, 040901(R) (2018).
[44] T. Divoux, C. Barentin, and S. Manneville, Soft Matter **7**, 9335 (2011).
[45] K. Baumgarten and B. P. Tighe, Soft Matter **13**, 8368 (2017).
[46] A. Ikeda, L. Berthier, and P. Sollich, Soft Matter **9**, 7669 (2013).
[47] V. V. Vasisht, G. Roberts, and E. Del Gado, arXiv:1709.08717.
[48] A. D. S. Parmar, S. Kumar, and S. Sastry, Phys. Rev. X **9**, 021018 (2019).
[49] J. D. Weeks, D. Chandler, and H. C. Andersen, J. Chem. Phys. **54**, 5237 (1971).
[50] P. Chaudhuri, L. Berthier, and L. Bocquet, Phys. Rev. E **85**, 021503 (2012).
[51] P. J. Steinhardt, D. R. Nelson, and M. Ronchetti, Phys. Rev. B **28**, 784 (1983).
[52] S. Sastry, P. G. Debenedetti, and F. H. Stillinger, Nature (London) **393**, 554 (1998).
[53] F. H. Stillinger, Science **267**, 1935 (1995).
[54] M. Mosayebi, P. Ilg, A. Widmer-Cooper, and E. Del Gado, Phys. Rev. Lett. **112**, 105503 (2014).
[55] S. Ashwin, Y. Brumer, D. R. Reichman, and S. Sastry, J. Phys. Chem. B **108**, 19703 (2004).
[56] S. Alexander, Phys. Rep. **296**, 65 (1998).
[57] M. Wyart, S. R. Nagel, and T. A. Witten, Europhys. Lett. **72**, 486 (2005).
[58] C. F. Schreck, N. Xu, and C. S. O'Hern, Soft Matter **6**, 2960 (2010).
[59] C. E. Maloney and A. Lemaître, Phys. Rev. E **74**, 016118 (2006).
[60] P. Chaudhuri, L. Berthier, and W. Kob, Phys. Rev. Lett. **99**, 060604 (2007).
[61] L. Berthier, P. Charbonneau, E. Flenner, and F. Zamponi, Phys. Rev. Lett. **119**, 188002 (2017).
[62] R. G. Larson, *The Structure and Rheology of Complex Fluids*, Topics in Chemical Engineering Vol. 150 (Oxford University Press, New York, 1999).
[63] B. P. Tighe, Phys. Rev. Lett. **107**, 158303 (2011).
[64] C. H. Rycroft, Chaos **19**, 041111 (2009).
[65] P. J. Steinhardt, D. R. Nelson, and M. Ronchetti, Phys. Rev. Lett. **47**, 1297 (1981).
[66] M. Mosayebi, E. Del Gado, P. Ilg, and H. C. Öttinger, J. Chem. Phys. **137**, 024504 (2012).

[67] C. P. Royall and S. R. Williams, Phys. Rep. **560**, 1 (2015).
[68] P. Ronceray and P. Harrowell, Soft Matter **11**, 3322 (2015).
[69] A. Nicolas, J.-L. Barrat, and J. Rottler, Phys. Rev. Lett. **116**, 058303 (2016).
[70] C. E. Maloney and M. O. Robbins, J. Phys.: Condens. Matter **20**, 244128 (2008).
[71] F. Puosi, J. Olivier, and K. Martens, Soft Matter **11**, 7639 (2015).
[72] F. Puosi, J. Rottler, and J.-L. Barrat, Phys. Rev. E **89**, 042302 (2014).
[73] E. Irani, P. Chaudhuri, and C. Heussinger, Phys. Rev. Fluids **4**, 074307 (2019).
[74] J. Colombo and E. Del Gado, J. Rheol. **58**, 1089 (2014).
[75] N. Hoh and R. Zia, J. Fluid Mech. **785**, 189 (2015).
[76] Y. Su, J. W. Swan, and R. N. Zia, J. Chem. Phys. **146**, 124903 (2017).
[77] T. Soddemann, B. Dünweg, and K. Kremer, Phys. Rev. E **68**, 046702 (2003).
[78] D. Frenkel and B. Smit, *Understanding Molecular Simulation: From Algorithms to Applications*, Vol. 1 (Academic Press, London, 2001).
[79] V. V. Vasisht, M. L. Goff, K. Martens, and J.-L. Barrat, arXiv:1812.03948.
[80] S. Plimpton, J. Comput. Phys. **117**, 1 (1995).
[81] R. L. Moorcroft and S. M. Fielding, Phys. Rev. Lett. **110**, 086001 (2013).
[82] K. M. Salerno, C. E. Maloney, and M. O. Robbins, Phys. Rev. Lett. **109**, 105703 (2012).
[83] A. Barbot, M. Lerbinger, A. Hernandez-Garcia, R. García-García, M. L. Falk, D. Vandembroucq, and S. Patinet, Phys. Rev. E **97**, 033001 (2018).
[84] D. Evans and G. Morriss, *Statistical Mechanics of Nonequilibrium Liquids* (Cambridge University Press, New York 2008).